

## Nanoparticle Catalyst Preparation Using Pulsed Arc Plasma Deposition

Satoshi Hinokuma,<sup>a, b, c</sup> Satoshi Misumi,<sup>a</sup> Hiroshi Yoshida<sup>b</sup> and Masato Machida,<sup>a, b\*</sup>

<sup>a</sup>*Department of Applied Chemistry and Biochemistry,*

*Graduate School of Science and Technology, Kumamoto University,*

*2-39-1 Kurokami, Chuo, Kumamoto, 860-8555 Japan*

<sup>b</sup>*Unit of Elements Strategy Initiative for Catalysts & Batteries,*

*Kyoto University, 1-30 Goryo-Ohara, Nishikyo, Kyoto 615-8245 Japan*

<sup>c</sup>*Japan Science and Technology Agency, Precursory Research for Embryonic Science and*

*Technology, 4-1-8 Honcho, Kawaguchi, Saitama, 332-0012 Japan*

### CORRESPONDING AUTHOR:

Prof. Masato Machida

Department of Applied Chemistry and Biochemistry,

Graduate School of Science and Technology,

Kumamoto University,

2-39-1 Kurokami, Chuo, Kumamoto, 860-8555 Japan

TEL/FAX: +81-96-342-3651

E-mail: machida@kumamoto-u.ac.jp

## Abstract

A novel nanoparticle preparation technique using pulsed arc plasma deposition has been developed as a dry catalyst preparation process in complete contrast to conventional wet processes. An overview of the principle, fundamental features of the technique and a discussion of the recent progress are presented using examples from our recent publications. The potential to prepare several types of supported metal and metal oxide catalysts with higher activities at minimum metal loadings is also highlighted.

Keywords: Pulsed arc plasma process, supported catalysts, metals, nanoparticles

## 1. Introduction

The most common techniques for the preparation of supported metal/metal oxide catalysts are wet processes (including impregnation and precipitation), which are usually employed for practical and economic reasons. In contrast, dry processes (including chemical/physical vapour deposition, sputtering and ion implantation), which are typically applied in the rapidly emerging field of semiconductor technology, remain limited as catalyst preparation techniques. Although the scientific basis of dry processes is certainly important from a fundamental viewpoint, dry processes that enable the use of powdered catalyst materials for practical applications are not available. One exceptional case is catalyst preparation using plasmas.<sup>1-4</sup> Various thermal and cold plasmas, including plasma jets, DC coronas, arcs, glow discharges, radio frequencies and microwaves, have been applied to the generation of ultrafine particles, preparation of supported catalysts and/or modification of catalyst surfaces. The potential merits of using plasmas are as follows<sup>3</sup>: (1) preparation of highly dispersed active species; (2) reduced energy requirements; (3) enhanced catalyst activation, selectivities and lifetimes and (4) shortened preparation times.

Among these plasma processes, pulsed cathodic arc plasma is promising as a simple and innovative approach that enables the deposition of metal nanoparticles or nanofilms from bulk metals or other electronic conducting materials.<sup>5-21</sup> A wide variety of nanoparticles have been successfully prepared to date using metals such as Fe,<sup>11</sup> Cu,<sup>11, 20</sup> Rh,<sup>6</sup> Pd,<sup>5, 9</sup> Pt,<sup>5, 7, 12, 14, 15</sup> Au,<sup>13, 21</sup> Ce<sup>10</sup> and carbon materials.<sup>16-19</sup> The most important feature of pulsed cathodic arc plasma is its applicability for the preparation of powdered supported catalysts and photocatalysts. This technique enables the one-step deposition of catalyst nanoparticles on

various support powders, which is in complete contrast to the multi-step preparation required for conventional wet impregnation processes. The as-prepared supported catalysts are characterised by highly dispersed and uniform metallic nanoparticles and thus achieve high catalytic activity. In this perspective article, we first describe the fundamentals of the pulsed arc plasma deposition technique and outline its advantages as a catalyst preparation tool. The structures and catalytic behaviour of the as-prepared nanoparticle catalysts are then described using several examples from our recent publications,<sup>5-11</sup> including both monometallic and bimetallic systems consisting of precious and nonprecious metals. The nonprecious metal catalysts may be used as substitutes for the precious metal catalysts currently used for selected elementary reactions in automotive emission control. Finally, future opportunities and challenges are also addressed.

## 2. Principle and apparatus

Figure 1 shows a schematic and a photograph of the experimental setup for nanoparticle catalyst preparation using pulsed arc plasma deposition. The apparatus consists of a vacuum chamber with a turbomolecular pumping system, arc discharge sources (Ulvac Inc., ARL-300) and a powder container with a rotating stirring mechanism. In the arc discharge source unit, a columnar cathode, an insulator tube, a trigger electrode and a cylindrical anode are arranged coaxially. A 10-mm-diameter and 17-mm-long metal rod of the target material connected to a DC supply is used as the cathode. The cylindrical anode is connected to the ground and the trigger electrode to a pulsed power supply. An electrolytic capacitor for charge and discharge is connected between the cathode and the ground. Application of a 3 kV pulse

to the trigger electrode causes an electronic breakdown between the trigger and cathode electrodes, which ignites pulsed arc discharges with a period of 0.1 to 0.2 ms between the cathode and the anode. The peak current of the discharges ranges from 2 to 6 kA. Due to the high spatiotemporal energy density, the metal on the cathode surface is immediately vapourised and ionised, resulting in the ejection of plasma. The very large arc discharge current through the cathode also induces a strong circumferential magnetic field that accelerates the metal ions and electrons in the ejected plasma via the Lorentzian force toward the powder container, where they are effectively collected. After the metal ions collide with the support powders, they lose their kinetic energy as they diffuse on the surface and are ultimately deposited as nanoparticles. During the repeated pulsing of the arc plasma, the support powders in the rotating Teflon container (diameter: 10 cm) are stirred using a scraper to ensure the homogeneous deposition of the nanoparticles.

Table 1 compares the characteristic features of pulsed arc plasma deposition to those of other dry processes for metal deposition (electron beam deposition and magnetron sputtering). Unlike these other processes, the metal ion species generated using the pulsed arc plasma technique have much higher kinetic energies and thus interact to a greater extent with the substrate surface. The resulting high adhesion forces stabilise the as-deposited nanoparticles against agglomeration. The pulsed arc plasma technique is therefore more efficient for nanoparticle formation than these other dry processes, which are more suitable for film growth applications. In addition, the as-deposited particles obtained with pulsed arc plasma deposition are nanoscale in size with a narrow size distribution, and the particle size can be readily controlled by varying the discharge parameters as described below. The

deposition density can also be controlled by varying the number of pulses while maintaining the same particle size. These features are extremely useful for studying the catalytic properties of a wide variety of metals and metal oxide nanoparticles with nearly uniform sizes.

A typical process for the pulsed arc plasma preparation of nanoparticle catalysts is as follows. Prior to arc plasma generation, the vacuum chamber is filled with N<sub>2</sub> and evacuated below  $1 \times 10^{-3}$  Pa overnight in order to remove water and gases adsorbed on the support powders in the container. A pulsed arc plasma with a period of 0.2 ms and a current amplitude of 2 kA is generated with a frequency of 1~2 Hz. The plasma thus ejected from the cathode enters into the container filled with the stirred support powders (rotation rate: 60 rpm) at ambient temperature. Figure 2 plots typical data for the weight of the deposits versus the number of pulses when a Rh metal rod is used as the cathode. The weight of the nanoparticle deposits, which was monitored using a quartz crystal microbalance, increased nearly linearly with the number of pulses. The metal loading on the support powders can therefore be controlled by varying the number of arc discharge pulses. On the other hand, the particle size and deposition rate per unit shot are dependent on the input energy ( $E$ ), which is expressed by  $E = (1/2)CV^2$ , where  $C$  is the electric capacitance and  $V$  is the applied discharge voltage.

Figure 3a shows transmission electron microscopy (TEM) images of Rh nanoparticles directly pulsed arc plasma deposited on a TEM grid covered with microgrid carbon films ( $C = 360 \mu\text{F}$ ,  $V = 125 \text{ V}$  and  $E = 3 \text{ J}$ ). Highly dispersed Rh nanoparticles with a uniform size can be seen in the image. The corresponding high-resolution structural image and fast Fourier transform (FFT) pattern shown in Figures 3b and c, respectively, reveal that these nanoparticles are crystallised metallic Rh with the face-centred cubic structure. The histogram

analysis presented in Figure 3d ( $E = 3$  J) clearly suggests a very narrow size distribution ranging from 1 to 5 nm with an average size of  $2.4 \pm 1.1$  nm. When the input energy was increased to 6 and 29 J, however, the particles size distribution becomes broadened and shifted toward larger sizes. Therefore, for catalyst preparation, an input energy  $E = 3$  J is typically employed. It should also be pointed out that higher input energies lead to frequent ejections of molten metal droplets from the cathode that are deposited as very large metal grains of more than several  $\mu\text{m}$  in diameter, which should be excluded for catalytic applications. Importantly, the particle size and histogram data are nearly the same when other metal cathodes, such as Pt and/or Pd, are used under the same conditions. However, the formation of molten metal droplets tends to be more frequent for metals with lower melting points. It should also be noted that the rate of deposition can be controlled without affecting the particles size by varying the pulsing frequency. As can be deduced from the operation mechanism shown in Figure 1a, the ejected plasmas reach only the top surfaces of the support powders. As a result, an appropriately engineered powder stirring mechanism is necessary for achieving the uniform deposition of metal nanoparticles on the surfaces of the support powders. In addition, this method cannot deposit nanoparticles directly inside the pores of materials with structural porosity and/or textural porosity, such as zeolites, mesoporous materials and porous agglomerates.

### 3. Preparation of platinum-group metal nanoparticles

This preparation technique was first applied to Pt/ $\text{Al}_2\text{O}_3$  catalysts. To confirm the influence of the support materials, TEM images of unsupported and  $\gamma$ - $\text{Al}_2\text{O}_3$ -supported Pt nanoparticles

were obtained and are shown in Figure 4. Here the unsupported Pt nanoparticles were as-deposited directly on a TEM grid covered with microgrid carbon films. Unsupported Pt nanoparticles (Figure 4a) with an average size of  $2.6 \pm 0.7$  nm were formed that were similar to the Rh nanoparticles shown in Figure 3, and the structure image and FFT pattern were also consistent with the face-centred cubic structure of metallic Pt. On  $\gamma$ -Al<sub>2</sub>O<sub>3</sub>, hemispherical Pt particles with a size of approximately 2 nm were deposited, as shown in Figure 4b. Clearly, the particle size was nearly the same as that of Pt deposited on the surface of the microgrid carbon films, and this result was also verified when other powdered materials, such as ZrO<sub>2</sub>, CeO<sub>2</sub>, AlPO<sub>4</sub> and so on were used as supports. Nanoparticles prepared via pulsed arc plasma deposition are therefore nearly the same size independent of the support material. The Pt particle size was also determined from the Pt dispersion, which was determined using CO or H<sub>2</sub> chemisorption data assuming a certain particle shape. As-deposited Pt/Al<sub>2</sub>O<sub>3</sub> exhibited a metal dispersion of  $D_{\text{Pt}} = 0.60$ , which corresponds to a particle size of  $d = 1.9$  nm for hemispherical Pt crystallites. The lower calculated particle size compared to those observed by TEM may suggest the presence of smaller particles that are invisible in the TEM images.

As-prepared samples were also characterized using X-ray photoelectron spectroscopy (XPS), extended X-ray absorption fine structure (EXAFS), and chemisorption technique. The comparison of the properties of supported metal catalysts prepared via pulsed arc plasma deposition and using conventional wet processes is of great interest. Hereafter, catalysts prepared via pulsed arc plasma deposition are denoted 'AP', and those prepared via conventional wet impregnation and post-calcination at 600 °C in air are referred to as 'imp'. As-deposited Pt/Al<sub>2</sub>O<sub>3</sub>(AP) exhibited a higher metal dispersion ( $D_{\text{Pt}} = 0.60$ ) compared to that



of the corresponding Pt/Al<sub>2</sub>O<sub>3</sub>(imp) impregnated catalyst ( $D_{Pt} = 0.38$ ).<sup>5</sup> The different Pt particles sizes can also be seen in the Fourier transforms of  $k^3$ -weighted Pt L<sub>III</sub>-edge EXAFS, as shown in Figure 5. Pt/Al<sub>2</sub>O<sub>3</sub>(AP) exhibited a much less intense peak for the Pt–Pt shell compared to that for Pt/Al<sub>2</sub>O<sub>3</sub>(imp) and Pt foil. Curve-fitting analyses yielded Pt coordination numbers of 2.4, 7.9 and 12.0 for Pt/Al<sub>2</sub>O<sub>3</sub>(AP), Pt/Al<sub>2</sub>O<sub>3</sub>(imp) and Pt foil, respectively. These values clearly indicate a high degree of coordinatively unsaturated (*cus*) Pt species in Pt/Al<sub>2</sub>O<sub>3</sub>(AP).

Pd nanoparticles can also be deposited on  $\gamma$ -Al<sub>2</sub>O<sub>3</sub> using AP. Unlike for Pt, however, the as-deposited Pd is partly oxidised when exposed to ambient air, as evidenced by the appearance of a Pd–O shell in the Fourier transform of the  $k^3$ -weighted Pd K-edge EXAFS spectrum (Figure 5). Nevertheless, the second coordination peaks due to Pd–O–Pd shells are not clear compared to those for Pd/Al<sub>2</sub>O<sub>3</sub>(imp), suggesting again the presence of *cus* Pd oxides. It should be noted that metallic Pd species are still present in Pd/Al<sub>2</sub>O<sub>3</sub>(AP), whereas Pd/Al<sub>2</sub>O<sub>3</sub>(imp) is composed only of Pd oxide. This is also confirmed by Pd3d XPS results.<sup>5</sup> The higher fraction of metallic states is another important characteristic of AP catalyst preparation because it enables one-step preparation of metallic nanoparticles in a highly dispersed state without the need for reduction.

The thermal stability of the catalysts prepared via AP was also considered from a practical perspective. Table 2 compares the BET surface areas ( $S_{BET}$ ) and metal dispersions for supported Pt and Pd catalysts prepared via arc plasma (AP) deposition and wet impregnation (imp) before and after thermal ageing at 900 °C.<sup>5, 7, 9</sup> When these metals were deposited on  $\gamma$ -Al<sub>2</sub>O<sub>3</sub>, substantial decreases in their dispersion occurred when the  $S_{BET}$  values

decreased after thermal ageing. It is likely that the sintering behaviour for the AP and imp catalysts was similar because metal-support interactions are not pronounced for  $\text{Al}_2\text{O}_3$  supports. The steeper decrease in the  $S_{\text{BET}}$  value for  $\text{CeO}_2$  resulted in more significant Pt sintering for  $\text{Pt/CeO}_2(\text{AP})$ , while  $\text{Pt/CeO}_2(\text{imp})$  did not exhibit such behaviour. The difference in the AP and imp catalysts in this case is associated with the Pt oxidation state as reported previously for  $\text{Pt/CeO}_2$  in automotive catalysts.<sup>22-24</sup>  $\text{Pt/CeO}_2(\text{imp})$  contains more Pt oxide that interacts with  $\text{CeO}_2$ , whereas the metallic Pt species that is abundant in  $\text{Pt/CeO}_2(\text{AP})$  interacts much less intensely. The  $\text{Pt/CeO}_2(\text{AP})$  catalyst is readily deactivated by sintering during thermal ageing due to the weaker metal-support interactions.<sup>7</sup> However, the situation is quite different when Pd is supported on  $\text{CeO}_2$ . In spite of the significant loss of  $S_{\text{BET}}$ , the Pd dispersion increased after thermal ageing. This result can be rationalised by strong metal-support interactions via Pd–O–Ce bonding on the  $\text{CeO}_2$  surface, which prevents the sintering of Pd oxide.<sup>9, 25</sup> In this regard,  $\text{CeO}_2$  is one of the most useful support materials for designing thermostable catalysts. In other words,  $\text{Pd/CeO}_2$  catalysts prepared via AP and imp exhibited similar thermal behaviour because of the strong interactions at the Pd– $\text{CeO}_2$  interface.

#### 4. Preparation of binary metal nanoparticles

Another main advantage of AP catalyst preparation is its applicability to bimetallic nanoparticles, which have been used as catalysts in many industrial processes because of their unique catalytic properties. From a scientific point of view, bimetallic nanoparticles supported on metal oxides have been extensively studied because their nanostructure and reactivity/selectivity change depending on their composition and method of preparation. The

apparatus for the present purpose included two cathodic arc sources, as shown in Figure 1b. It should be noted that different types of bimetallic nanoparticles can be prepared using synchronous or asynchronous generation of two plasmas from each AP source. When the two pulses are triggered by a single external input, the synchronous generation of two different plasmas is possible. On the other hand, two alternating pulses triggered by two external inputs generate two asynchronous plasmas from each source. Figure 6 schematically illustrates the event after metal ions in the plasma reach the substrate surface in each case. Under synchronous (syn) conditions, the two plasmas generated from two sources reach the substrate surface nearly simultaneously. After collision with the surface, the two metal species diffuse on the surface and collide with each other, leading to the deposition of bimetallic (composite) nanoparticles. When the two pulses are not synchronised (asyn), the situation is completely different; the metal species do not collide with one another because the period of the pulsed plasma is very short ( $<0.2$  ms) compared to the pulse interval ( $>0.5$  s). Consequently, the two metal species are deposited separately.

Figure 7 shows TEM images and energy dispersive X-ray analysis (EDX) results for Pd–Fe nanoparticles prepared using the synchronous and asynchronous AP modes.<sup>7</sup> In the case of synchronous pulsing, the as-deposited single nanoparticles contained both Pd and Fe (Pd: 33 wt%, Fe: 67 wt%), whereas the single nanoparticles prepared via asynchronous pulsing contained only Fe (Pd: 0 wt%, Fe: 100 wt%). Similarly, the EDX spectra for other Pd–Fe(asyn) single nanoparticles taken from different fields of view revealed the presence of only Pd. EXAFS analysis of Pd–Fe nanoparticles deposited on  $\gamma$ -Al<sub>2</sub>O<sub>3</sub> also revealed the different local structure of the Pd–Fe nanoparticles deposited on  $\gamma$ -Al<sub>2</sub>O<sub>3</sub>. Figure 8 presents

Fourier-transforms and curve-fitting results for Pd K-edge EXAFS for spectra of the Pd–Fe/Al<sub>2</sub>O<sub>3</sub> samples along with two reference materials (see Table S1 in the ESI† for fitting results). Because the phase shift was not corrected, the observed peaks are shifted to shorter values with respect to the fitted atomic distances. The intense peak at 2.01 Å and the weak peak at 2.74 Å are attributed to the Pd–O and Pd–Pd shells, respectively, and are indicative of the partial oxidation of the Pd metal. However, the shoulder of the weak peak at approximately 2.70 Å, which was observed for Pd–Fe/Al<sub>2</sub>O<sub>3</sub>(syn) only, was fitted when the contribution of the Fe<sub>3</sub>Pd<sub>1</sub> Pd–Fe shell along with a Pd–Pd shell was taken into consideration. These results clearly demonstrate that bimetallic composite nanoparticles containing both Pd and Fe were formed by synchronising two pulsed arc plasmas. In accordance with the structural differences, the Pd–Fe bimetallic nanoparticles in Pd–Fe/Al<sub>2</sub>O<sub>3</sub>(syn) were found to stabilise the metallic states of the Pd and Fe and exhibit higher catalytic activity for CO oxidation than that of Pd–Fe/Al<sub>2</sub>O<sub>3</sub>(asyn).<sup>7</sup>

## 5. Application to nonprecious metals

Unlike precious metals, it is impossible to prepare metal nanoparticles from irreducible metal oxides and salts (such as Al, Zr, W and lanthanides) via high-temperature H<sub>2</sub> reduction. For such species, however, the AP process is a convenient and powerful tool for preparing metal nanoparticles. For instance, although a wide variety of synthetic techniques have been developed to prepare cerium oxide nanoparticles,<sup>26</sup> they cannot be reduced fully to the corresponding metallic nanoparticles using H<sub>2</sub>. By contrast, AP enables one-step deposition of metallic nanoparticles from bulk Ce metal.<sup>10</sup> As can be seen in the high-angle annular dark

field scanning electron transmission microscopy (HAADF-STEM) images shown in Figure 9, Ce nanoparticles as deposited on Al<sub>2</sub>O<sub>3</sub> via AP appeared as bright dots with a size of less than 1 nm. All of the Ce particles deposited using the AP process under vacuum were oxidised when exposed to ambient air; thus the nanoparticles were composed of oxides. Considering their size (<1 nm), these sub-nanoparticles were atomic clusters closely equivalent to the unit cell parameter of CeO<sub>2</sub> ( $a = 0.54$  nm). The considerable presence of Ce<sup>3+</sup> (44%) was suggested by the Ce L<sub>III</sub>-edge XANES spectrum, whereas only 12% Ce<sup>3+</sup> was indicated for the Ce/Al<sub>2</sub>O<sub>3</sub> sample prepared using the conventional wet impregnation method. These results revealed that highly dispersed cerium oxide sub-nanoparticles containing *cus* Ce in a lower oxidation state (3+) were deposited on  $\gamma$ -Al<sub>2</sub>O<sub>3</sub>.

More interestingly, Ce/Al<sub>2</sub>O<sub>3</sub>(AP) exhibited unexpected catalytic activity for CO oxidation, as shown in Figure 10. During the temperature ramp at 10 °C·min<sup>-1</sup>, the light-off of a stream of 0.1% CO, 1.25% O<sub>2</sub> and He balance was observed at 250 °C for Ce/Al<sub>2</sub>O<sub>3</sub>(AP), while it was >600 °C for the impregnated Ce/Al<sub>2</sub>O<sub>3</sub>(imp) sample. In addition, thermal ageing at 900 °C caused the deactivation of Ce/Al<sub>2</sub>O<sub>3</sub>(imp), but enhanced the activity of Ce/Al<sub>2</sub>O<sub>3</sub>(AP). The different catalytic behaviour of the two catalysts is in accordance with the dependence of the CO oxidation rate on the partial pressures of CO and O<sub>2</sub>; Ce/Al<sub>2</sub>O<sub>3</sub>(imp) exhibited partial orders with respect to CO and O<sub>2</sub> of ~1.0 and ~0.0, respectively, in agreement with the Mars-van Krevelen mechanism as previously reported for the oxidation of CO over CeO<sub>2</sub>.<sup>27</sup> On the other hand, Ce/Al<sub>2</sub>O<sub>3</sub>(AP) exhibited positive orders with respect to both CO (~0.5) and O<sub>2</sub> (~0.2) and approximately a two-fold higher activation energy ( $E_a$ ) than that of Ce/Al<sub>2</sub>O<sub>3</sub>(imp). These results may suggest that the highly dispersed *cus* Ce sites in

Ce/Al<sub>2</sub>O<sub>3</sub>(AP) affect the adsorption of both CO and O<sub>2</sub> on the surface. Although details of the reaction mechanism remain unclear, this result implies that nanoparticles of nonprecious metals prepared via AP exhibit catalytic activities that are different from those of catalysts prepared via conventional wet impregnation.

The application of the dual-mode AP process to various nonprecious metal systems is also promising. For instance, Fe–Cu/CeO<sub>2</sub> catalysts with a small Fe/Cu loading (0.2 wt% each) have been prepared.<sup>11</sup> As was the case for the Pd–Fe bimetallic system described above,<sup>10</sup> synchronising two plasma sources (Fe and Cu) triggered by a single external input deposited bimetallic (composite) nanoparticles. The particle size of the as-deposited Fe–Cu bimetal was approximately 2 nm, which was similar to those of nanoparticles consisting of Fe and Cu alone. Figure 11 compares the light-off curves for CO oxidation over Fe/CeO<sub>2</sub>(AP), Cu/CeO<sub>2</sub>(AP), Fe–Cu/CeO<sub>2</sub>(AP) and Fe–Cu/CeO<sub>2</sub>(imp) before and after the samples were thermally aged at 900 °C. The activity of the as-prepared catalysts increased in the following order: Fe/CeO<sub>2</sub>(AP) < Fe–Cu/CeO<sub>2</sub>(AP) < Cu/CeO<sub>2</sub>(AP) < Fe–Cu/CeO<sub>2</sub>(imp). However, the thermally aged samples exhibited completely different catalytic behaviour. Although Fe/CeO<sub>2</sub>(AP) was significantly deactivated, the other samples containing Cu showed enhanced activities despite the significant loss of surface area from 170 m<sup>2</sup>·g<sup>-1</sup> to less than 10 m<sup>2</sup>·g<sup>-1</sup> because of the sintering of CeO<sub>2</sub>. The extent of the activity enhancement was most obvious for Fe–Cu/CeO<sub>2</sub>(AP), which exhibited the highest activity after thermal ageing.

The catalytic activity was closely associated with the oxidation state and dispersion of Cu and Fe. Although the AP process under vacuum yielded metallic nanoparticles, they were oxidised during calcination in air. As revealed by XPS analysis, Fe–Cu/CeO<sub>2</sub>(AP) after

thermal ageing at 900 °C consisted of Fe<sup>3+</sup> and Cu<sup>+</sup>, whereas Fe<sup>2+</sup> and Cu<sup>2+</sup> were abundant in the catalyst prepared via wet impregnation (Fe–Cu/CeO<sub>2</sub>(imp)). The different oxidation states of Cu influenced the CO adsorption behaviour of the catalysts. Although the as-prepared Fe, Cu and Fe–Cu/CeO<sub>2</sub>(AP) catalysts exhibited only very weak CO chemisorption, thermal ageing led to very strong CO adsorption on Cu<sup>+</sup> sites on the CeO<sub>2</sub> surface. It has been suggested that Cu is present on CeO<sub>2</sub> in a variety of forms depending on the preparation method and conditions: bulk Cu oxide, isolated Cu ions incorporated in the CeO<sub>2</sub> lattice and/or surface Cu ions. According to the density functional theory (DFT) calculations for the structure of the Cu-doped CeO<sub>2</sub> (111) surface, Cu is stable both as an adsorbed atom (Cu<sup>+</sup>) on the surface and as a dopant (Cu<sup>2+</sup>) in the CeO<sub>2</sub> surface region.<sup>28</sup> Considering that the Cu<sup>+</sup> species on the surface are the CO adsorption sites, Cu–CeO<sub>2</sub> interfacial bonding is thought to play a primary role in the high dispersion of Cu<sup>+</sup> species after thermal ageing. The role of Fe is thus to promote Cu<sup>+</sup> dispersion on the CeO<sub>2</sub> surface through the formation of Fe<sup>3+</sup>–Cu<sup>+</sup> oxide moieties bound to the CeO<sub>2</sub> surface. These Fe<sup>3+</sup>–Cu<sup>+</sup> oxide species are formed from bimetallic nanoparticles deposited via dual-mode AP, but cannot be readily generated in catalysts prepared via wet impregnation, likely due to the very low metal loading (0.2 wt%). These results demonstrate that Cu loaded on CeO<sub>2</sub> is a promising alternative candidate for precious metal catalysts due to its efficient activity for CO oxidation.<sup>29-33</sup> The high dispersion of Cu as a result of the interactions with CeO<sub>2</sub> and other dopants is believed to play a key role in the catalytic performance. In this regard, the AP catalyst preparation technique is beneficial for the deposition of small amounts of several different metal species on CeO<sub>2</sub>.

#### 4. Remarks and perspectives

It is well-known that future research in energy and environmental catalysis should be mainly oriented towards the reduction of precious metal use because such metals are expensive and have a limited supply. The key benefit of the AP technique is the very simple one-step deposition of metal nanoparticles from bulk metals on powdered support surfaces with uniform particles sizes and high catalytic activity. These features are expected to lead to the development of novel and innovative catalyst preparation processes that enable reduced metal loadings with retention of catalytic performance. In addition, the partial or total substitution of precious metals by more abundant alternative metals is an ideal solution with a more striking impact. In this regard, composite nanoparticles prepared by synchronising multi-AP sources offer an interesting approach to the construction of novel active sites on strongly interacting support materials, such as CeO<sub>2</sub>. The AP catalyst preparation technique described herein is still in the fundamental stage of development and applicable only to batch operations. However, the installation of multi-AP sources, a load-lock chamber, a powder supply mechanism and a powder tray transfer unit will enable the continuous production of supported catalyst powders on a commercial scale. Efficient powder stirring by means of mechanical or ultrasonic vibration will also be necessary for the homogeneous deposition of nanoparticle active components on powder supports.

#### Acknowledgements

This study was supported by the ‘Elements Science and Technology Project’ and by the ‘Elements Strategy Initiative for Catalysts & Batteries (ESICB)’ supported by MEXT program



‘Elements Strategy Initiative to Form Core Research Center’ (since 2012), MEXT; Ministry of Education Culture, Sports, Science and Technology, Japan.

## Notes and references

1. M. Boutonnet Kizling and S. G. Järås, *Appl. Catal. A: Gen.*, 1996, **147**, 1-21.
2. Z. R. Ismagilov, O. Y. Podyacheva, O. P. Solonenko, V. V. Pushkarev, V. I. Kuz'min, V. A. Ushakov and N. A. Rudina, *Catal. Today*, 1999, **51**, 411-417.
3. C.-j. Liu, G. P. Vissokov and B. W. L. Jang, *Catal. Today*, 2002, **72**, 173-184.
4. H. Shim, J. Phillips, I. M. Fonseca and S. Carabinerio, *Appl. Catal. A: Gen.*, 2002, **237**, 41-51.
5. S. Hinokuma, K. Murakami, K. Uemura, M. Matsuda, K. Ikeue, N. Tsukahara and M. Machida, *Top. Catal.*, 2009, **52**, 2108-2111.
6. S. Hinokuma, M. Okamoto, E. Ando, K. Ikeue and M. Machida, *Catal. Today*, 2011, **175**, 593-597.
7. S. Hinokuma, M. Okamoto, E. Ando, K. Ikeue and M. Machida, *Bull. Chem. Soc. Jpn.*, 2012, **85**, 144-149.
8. S. Hinokuma, Y. Katsuhara, E. Ando, K. Ikeue and M. Machida, *Catal. Today*, 2013, **201**, 92-97.
9. S. Hinokuma, H. Fujii, Y. Katsuhara, K. Ikeue and M. Machida, *Catal. Sci. Technol.*, 2014, **4**, 2990-2996.
10. S. Hinokuma, H. Kogami, N. Yamashita, Y. Katsuhara, K. Ikeue and M. Machida, *Catal. Commun.*, 2014, **54**, 81-85.
11. S. Hinokuma, N. Yamashita, Y. Katsuhara, H. Kogami and M. Machida, *Catal. Sci. Technol.*, 2015, **5**, DOI: 10.1039/c1035cy00370a.
12. Y. Agawa, S. Endo, M. Matsuura and Y. Ishii, *ECS Transactions*, 2012, **50**, 1271-1276.

13. T. Fujitani and I. Nakamura, *Angew. Chem. Int. Ed.*, 2011, **50**, 10144-10147.
14. K. Qadir, S. H. Kim, S. M. Kim, H. Ha and J. Y. Park, *J. Phys. Chem. C*, 2012, **116**, 24054-24059.
15. S. H. Kim, C. H. Jung, N. Sahu, D. Park, J. Y. Yun, H. Ha and J. Y. Park, *Appl. Catal. A: Gen.*, 2013, **454**, 53-58.
16. T. Yoshitake, Y. Nakagawa, A. Nagano, R. Ohtani, H. Setoyama, E. Kobayashi, K. Sumitani, Y. Agawa and K. Nagayama, *Jpn. J. Appl. Phys.*, 2010, **49**, 015503.
17. K. Hanada, T. Yoshida, Y. Nakagawa and T. Yoshitake, *Jpn. J. Appl. Phys.*, 2010, **49**, 125503.
18. C. Qin and S. Coulombe, *Mater. Lett.*, 2006, **60**, 1973-1976.
19. A. V. Stanishevsky and E. L. Tochitsky, *J. Wide Bandgap Mater.*, 1996, **4**, 297-310.
20. A. S. Chaus, T. N. Fedosenko, A. V. Rogachev and E. Čaplovič, *Diamond Relat. Mater.*, 2014, **42**, 64-70.
21. B. Naik, S. M. Kim, C. H. Jung, S. Y. Moon, S. H. Kim and J. Y. Park, *Advanced Materials Interfaces*, 2014, **1**, 201300018.
22. Y. Nagai, K. Dohmae, K. Teramura, T. Tanaka, G. Guilera, K. Kato, M. Nomura, H. Shinjoh and S. Matsumoto, *Catal. Today*, 2009, **145**, 279-287.
23. Y. Nagai, K. Dohmae, Y. Ikeda, N. Takagi, T. Tanabe, N. Hara, G. Guilera, S. Pascarelli, M. A. Newton, O. Kuno, H. Jiang, H. Shinjoh and S. i. Matsumoto, *Angew. Chem. Int. Ed.*, 2008, **47**, 9303-9306.
24. Y. Nagai, T. Hirabayashi, K. Dohmae, N. Takagi, T. Minami, H. Shinjoh and S. i. Matsumoto, *J. Catal.*, 2006, **242**, 103-109.

25. S. Hinokuma, H. Fujii, M. Okamoto, K. Ikeue and M. Machida, *Chem. Mater.*, 2010, **22**, 6183-6190.
26. G. Adachi and T. Masui, in *Catalysis by ceria and related materials*, ed. A. Trovarelli, Imperial College Press, London, 2002, p. 51.
27. M. Breyse, M. Guenin, B. Claudel, H. Latreille and J. Véron, *J. Catal.*, 1972, **27**, 275-280.
28. Z. Yang, B. He, Z. Lu and K. Hermansson, *J. Phys. Chem. C*, 2010, **114**, 4486-4494.
29. W. Liu and M. Flytzanistephanopoulos, *J. Catal.*, 1995, **153**, 304-316.
30. M.-F. Luo, J.-M. Ma, J.-Q. Lu, Y.-P. Song and Y.-J. Wang, *J. Catal.*, 2007, **246**, 52-59.
31. L. Qi, Q. Yu, Y. Dai, C. Tang, L. Liu, H. Zhang, F. Gao, L. Dong and Y. Chen, *Appl. Catal. B: Environ.*, 2012, **119–120**, 308-320.
32. C.-Y. Shiau, M. W. Ma and C. S. Chuang, *Appl. Catal. A: Gen.*, 2006, **301**, 89-95.
33. D. Zhang, Y. Qian, L. Shi, H. Mai, R. Gao, J. Zhang, W. Yu and W. Cao, *Catal. Commun.*, 2012, **26**, 164-168.

Table 1 Features of dry processes for metal deposition

	Pulsed arc plasma	Electron-beam	Sputtering
Deposition mode	Intermittent	Continuous	Continuous
Deposition rate control	Pulse control $\sim 0.02 \text{ nm s}^{-1}$	Shutter control $\sim 1 \text{ nm s}^{-1}$	Shutter control $\sim 1 \text{ nm s}^{-1}$
Nanoparticle deposition and size	Easy <2 nm	Difficult >8 nm	Difficult –
Adhesion to substrate	Strong	Very weak	Weak

Table 2 Metal dispersion in Pt and Pd catalysts as-prepared using pulsed arc plasma deposition and after ageing

Catalyst <sup>a</sup>		$S_{\text{BET}}^b$ / $\text{m}^2 \cdot \text{g}^{-1}$	Dispersion <sup>c</sup> / %
Pt/Al <sub>2</sub> O <sub>3</sub> (AP)	fresh	134	60
	aged	80	23
Pt/Al <sub>2</sub> O <sub>3</sub> (imp)	fresh	126	38
	aged	75	11
Pd/Al <sub>2</sub> O <sub>3</sub> (AP)	fresh	134	41
	aged	71	24
Pd/Al <sub>2</sub> O <sub>3</sub> (imp)	fresh	135	54
	aged	68	8
Pt/CeO <sub>2</sub> (AP)	fresh	160	77
	aged	8	7
Pt/CeO <sub>2</sub> (imp)	fresh	97	70
	aged	7	53
Pd/CeO <sub>2</sub> (AP)	fresh	162	42
	aged	11	94
Pd/CeO <sub>2</sub> (imp)	fresh	116	58
	aged	11	74

<sup>a</sup> Metal loading: 0.4 wt%; ‘fresh’ refers to catalysts that were uncalcined (AP) and calcined at 600 °C for 3 h in air (imp), and ‘aged’ refers to catalysts after heating at 900 °C for 25 h in 10% H<sub>2</sub>O/air.

<sup>b</sup> BET surface area.

<sup>c</sup> Dispersion is expressed in terms of the molar ratio of the chemisorbed CO and loaded metal. The quantity of chemisorbed CO was determined using a pulse method at 50 °C.

## Figure captions

Figure 1. (a) Schematic of the pulsed arc plasma process for the deposition of metal nanoparticles, and (b) photograph of the experimental setup with dual arc plasma sources.

Figure 2. Weight of Rh deposits as a function of the number of arc plasma pulses. Input energy, 3 J and pulse frequency, 1 Hz.

Figure 3. (a) TEM image, (b) high-resolution structure image and (c) FFT pattern of unsupported Rh nanoparticles deposited using arc plasma with an input energy of 3 J and (d) size distributions of Rh nanoparticles deposited at different input energies of 3, 6 and 29 J.<sup>6</sup>

Figure 4. (a) TEM and high-resolution structure images and FFT pattern of unsupported Pt nanoparticles deposited on a TEM grid covered with microgrid carbon films. (b) TEM image of Pt nanoparticles deposited on  $\gamma$ -Al<sub>2</sub>O<sub>3</sub>. Arc plasma deposition with an input energy of 3 J.

Figure 5. (left) Fourier transforms of  $k^3$ -weighted Pt L<sub>III</sub>-edge EXAFS for (a) Pt/Al<sub>2</sub>O<sub>3</sub>(AP), (b) Pt/Al<sub>2</sub>O<sub>3</sub>(imp), (c) Pt foil and (d) PtO<sub>2</sub>. (right) Fourier transforms of  $k^3$ -weighted Pd K-edge EXAFS of as-prepared (a) Pd/Al<sub>2</sub>O<sub>3</sub>(AP), (b) Pd/Al<sub>2</sub>O<sub>3</sub>(imp), (c) PdO and (d) Pd foil.

Figure 6. Schematic of particle formation via the synchronous and asynchronous generation of two plasmas and surface diffusion of the atoms on a support material.

Figure 7. TEM images and EDX spectra of unsupported Pd–Fe nanoparticles prepared via (left) synchronous (syn) and (right) asynchronous (asyn) pulsing. Each EDX spectrum was taken from a circular region containing one nanoparticle.<sup>8</sup>

Figure 8. Fourier transforms of  $k^3$ -weighted Pd K-edge EXAFS of Pd–Fe/Al<sub>2</sub>O<sub>3</sub> prepared via synchronous (syn) and asynchronous (asyn) pulsed arc plasma deposition. PdO and Pd foil are shown as references.

Figure 9. Cs-corrected HAADF-STEM images of (a) Ce oxide sub-nanoparticles as deposited directly on  $\gamma$ -Al<sub>2</sub>O<sub>3</sub> and (b) bare  $\gamma$ -Al<sub>2</sub>O<sub>3</sub> grains.<sup>10</sup>

Figure 10. CO oxidation activity of 0.7 wt% (a) Ce/Al<sub>2</sub>O<sub>3</sub>(AP) and (b) Ce/Al<sub>2</sub>O<sub>3</sub>(imp) before and after thermal ageing at 900 °C for 25 h in 10% H<sub>2</sub>O/air.<sup>10</sup>

Figure 11. Temperature dependence of CO oxidation over Fe/CeO<sub>2</sub>(AP), Cu/CeO<sub>2</sub>(AP), Fe–Cu/CeO<sub>2</sub>(AP) and Fe–Cu/CeO<sub>2</sub>(imp) before and after the catalysts were thermally aged at 900 °C for 25 h in 10% H<sub>2</sub>O/air. Reaction conditions: 0.1% CO, 1.25% O<sub>2</sub>, He balance, W/F =  $5.0 \times 10^{-4}$  g·min·cm<sup>-3</sup>.<sup>11</sup>



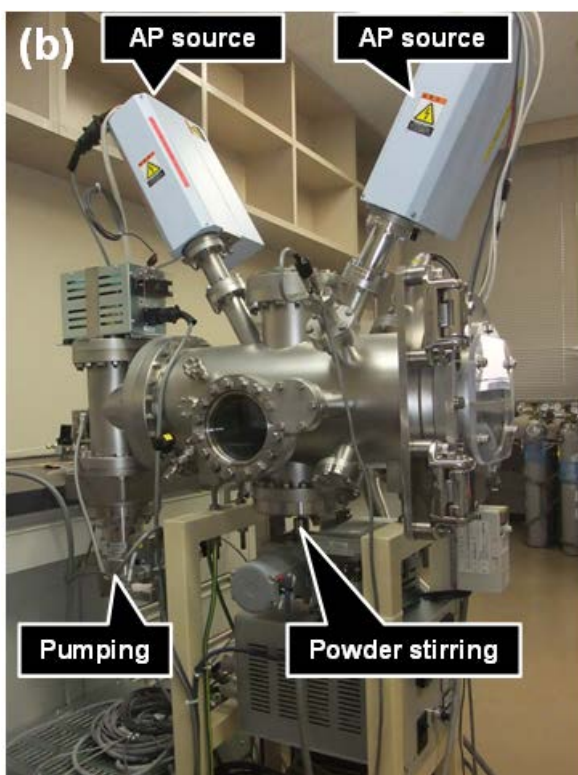
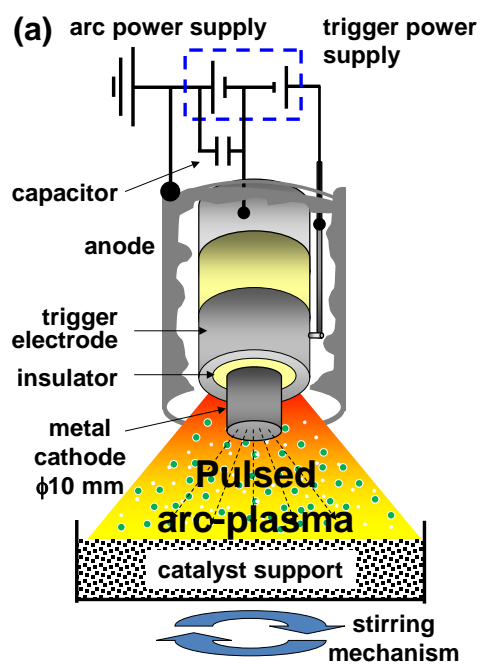


Figure 1. (a) Schematic of the pulsed arc plasma process for the deposition of metal nanoparticles, and (b) photograph of the experimental setup with dual arc plasma sources.

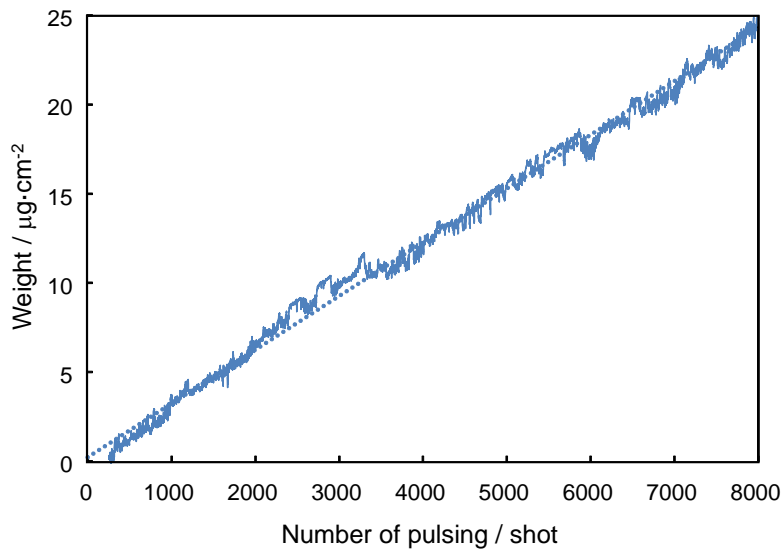


Figure 2. Weight of Rh deposits as a function of the number of arc plasma pulses. Input energy, 3 J and pulse frequency, 1 Hz.

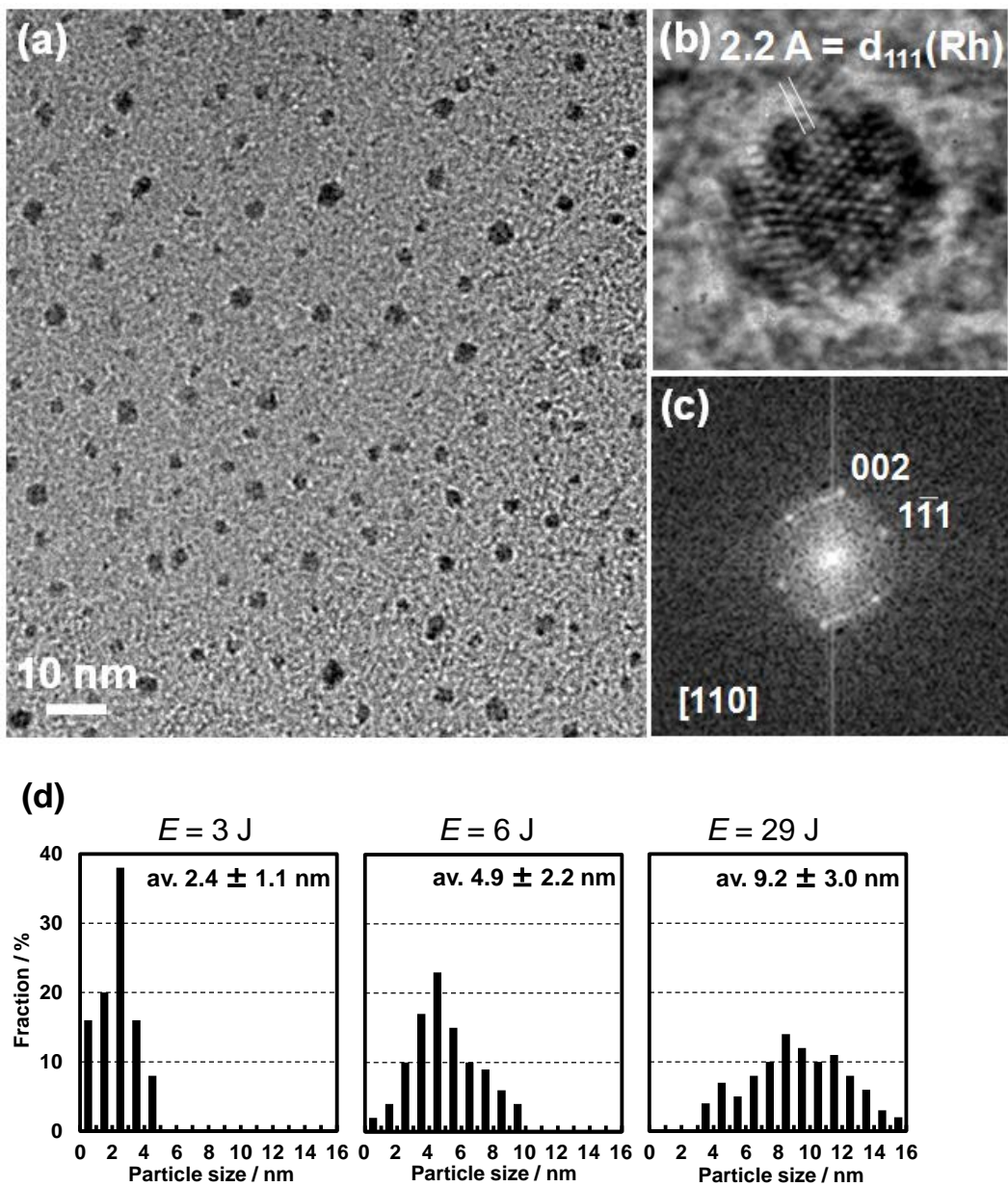


Figure 3. (a) TEM image, (b) high-resolution structure image and (c) FFT pattern of unsupported Rh nanoparticles deposited using arc plasma with an input energy of 3 J and (d) size distributions of Rh nanoparticles deposited at different input energies of 3, 6 and 29 J.<sup>6</sup>

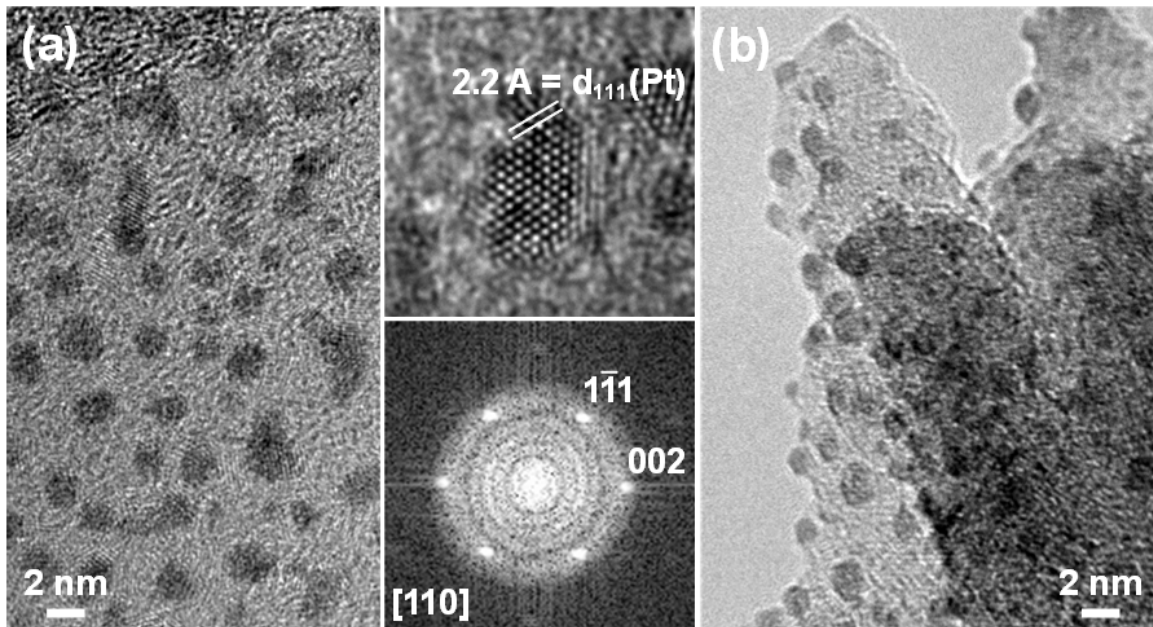


Figure 4. (a) TEM and high-resolution structure images and FFT pattern of unsupported Pt nanoparticles deposited on a TEM grid covered with microgrid carbon films. (b) TEM image of Pt nanoparticles deposited on  $\gamma$ -Al<sub>2</sub>O<sub>3</sub>. Arc plasma deposition with an input energy of 3 J.

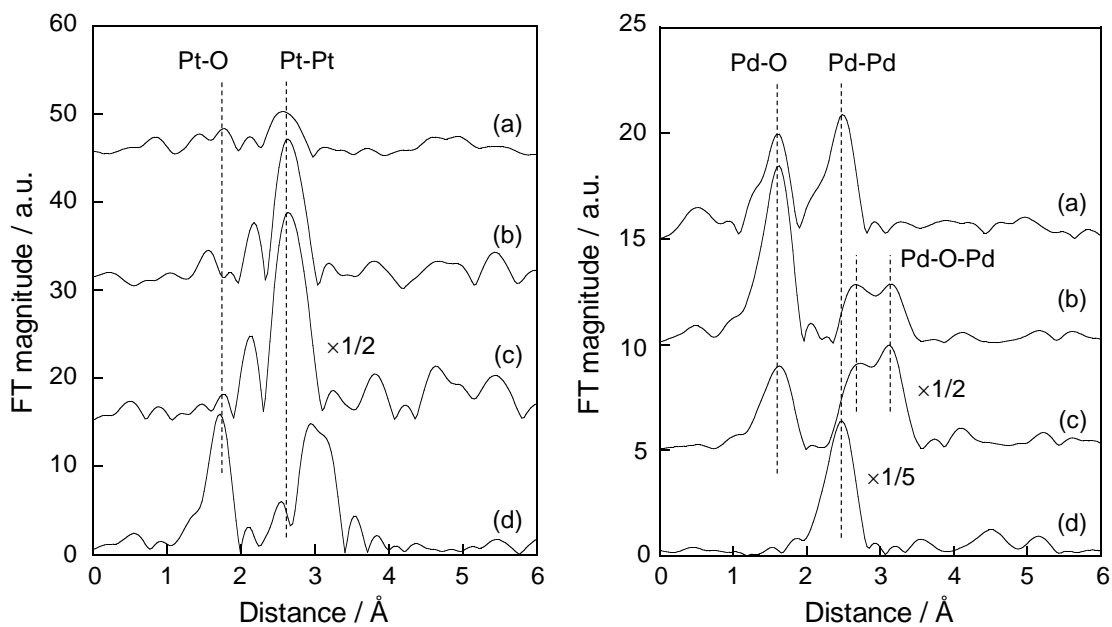


Figure 5. (left) Fourier transforms of  $k^3$ -weighted Pt L<sub>III</sub>-edge EXAFS for (a) Pt/Al<sub>2</sub>O<sub>3</sub>(AP), (b) Pt/Al<sub>2</sub>O<sub>3</sub>(imp), (c) Pt foil and (d) PtO<sub>2</sub>. (right) Fourier transforms of  $k^3$ -weighted Pd K-edge EXAFS of as-prepared (a) Pd/Al<sub>2</sub>O<sub>3</sub>(AP), (b) Pd/Al<sub>2</sub>O<sub>3</sub>(imp), (c) PdO and (d) Pd foil.

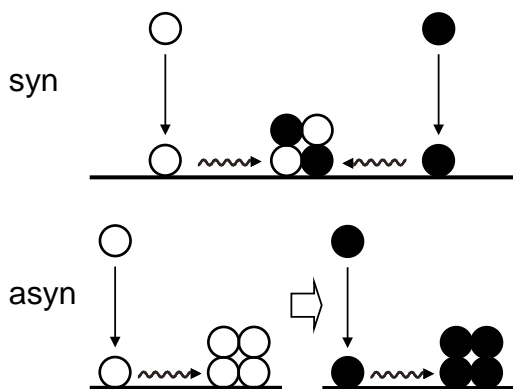


Figure 6. Schematic of particle formation via the synchronous and asynchronous generation of two plasmas and surface diffusion of the atoms on a support material.

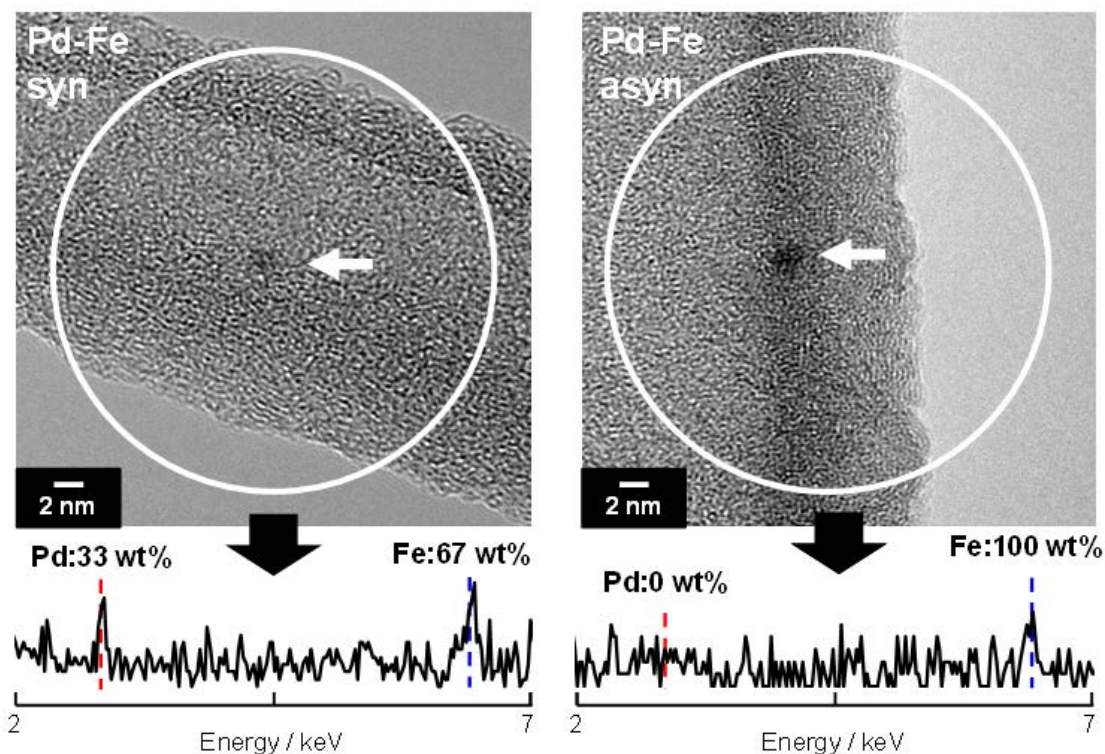


Figure 7. TEM images and EDX spectra of unsupported Pd–Fe nanoparticles prepared via (left) synchronous (syn) and (right) asynchronous (asyn) pulsing. Each EDX spectrum was taken from a circular region containing one nanoparticle.<sup>8</sup>

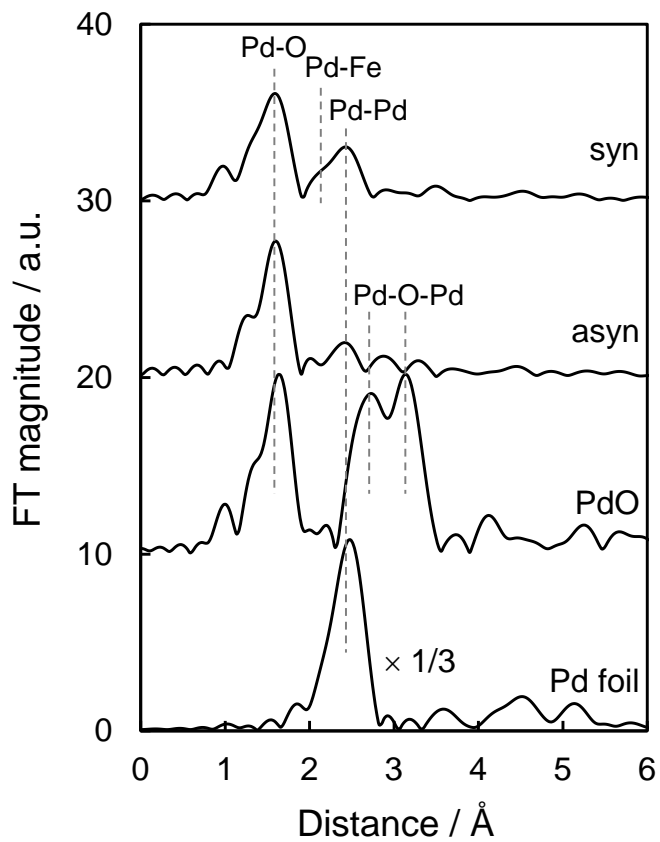


Figure 8. Fourier transforms of  $k^3$ -weighted Pd K-edge EXAFS of Pd-Fe/ $\text{Al}_2\text{O}_3$  prepared via synchronous (syn) and asynchronous (asyn) pulsed arc plasma deposition. PdO and Pd foil are shown as references.

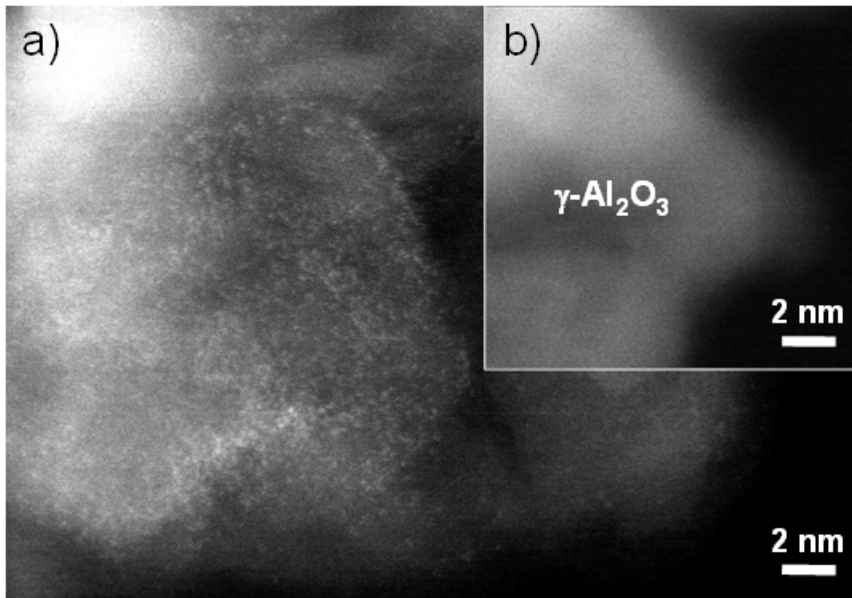


Figure 9. Cs-corrected HAADF-STEM images of (a) Ce oxide sub-nanoparticles as deposited directly on  $\gamma\text{-Al}_2\text{O}_3$  and (b) bare  $\gamma\text{-Al}_2\text{O}_3$  grains.<sup>10</sup>



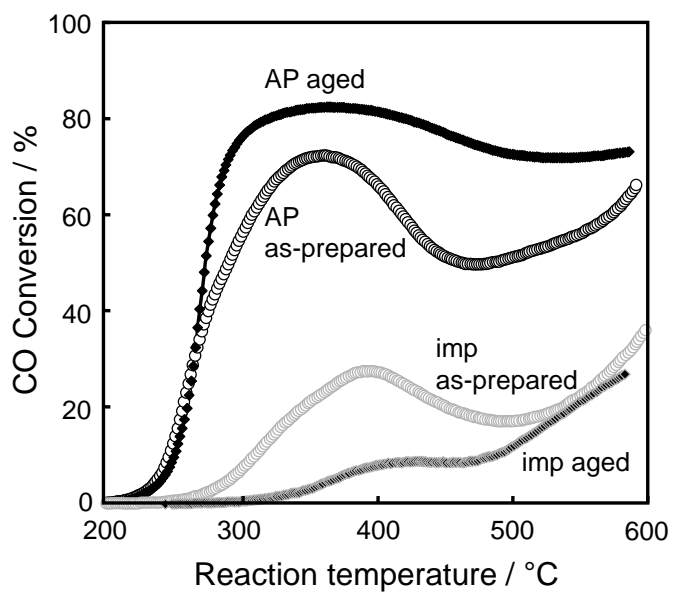


Figure 10. CO oxidation activity of 0.7 wt% (a)  $\text{Ce}/\text{Al}_2\text{O}_3(\text{AP})$  and (b)  $\text{Ce}/\text{Al}_2\text{O}_3(\text{imp})$  before and after thermal ageing at 900 °C for 25 h in 10%  $\text{H}_2\text{O}/\text{air}$ .<sup>10</sup>

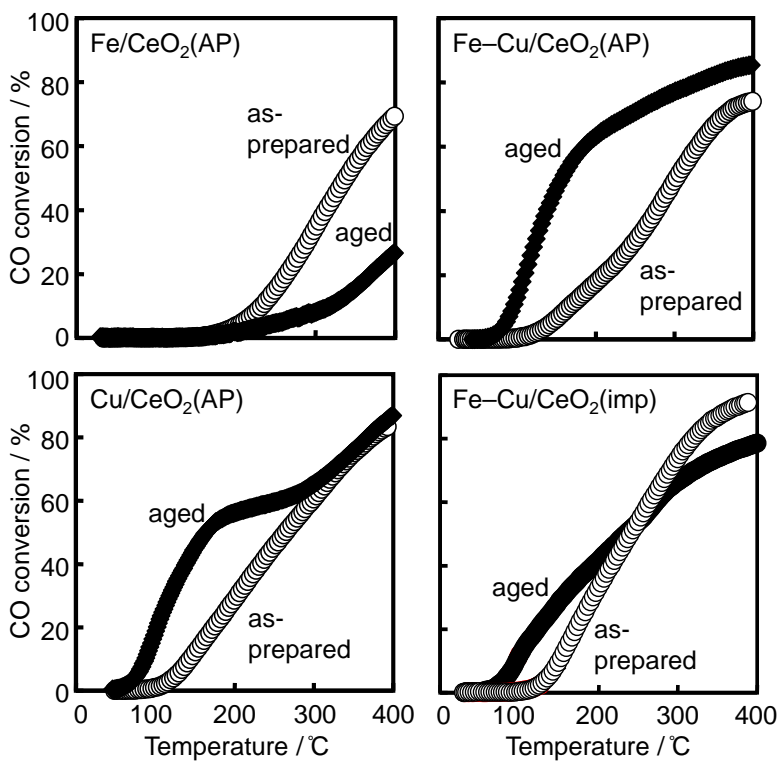


Figure 11. Temperature dependence of CO oxidation over Fe/CeO<sub>2</sub>(AP), Cu/CeO<sub>2</sub>(AP), Fe-Cu/CeO<sub>2</sub>(AP) and Fe-Cu/CeO<sub>2</sub>(imp) before and after the catalysts were thermally aged at 900 °C for 25 h in 10% H<sub>2</sub>O/air. Reaction conditions: 0.1% CO, 1.25% O<sub>2</sub>, He balance, W/F =  $5.0 \times 10^{-4}$  g·min·cm<sup>-3</sup>.<sup>11</sup>